Higher-order Lamb waves with quasi-zero surface displacement components on a GaAs piezoelectric plate

Muhammad Hamidullah, Céline Elie-Caille, Thérèse Leblois

Higher-order Lamb waves with quasi-zero surface displacement components on a GaAs piezoelectric plate

Muhammad Hamidullah, Céline Élie-Caille and Thérèse Leblois

FEMTO-ST Institute, CNRS UMR-6174, Université de Bourgogne Franche-Comté, 25000 Besançon, France

E-mail: muhammad.hamidullah@femto-st.fr

Received xxxxxx
Accepted for publication xxxxxx
Published xxxxxx

Abstract

Higher-order Lamb waves with quasi-zero surface displacement components are reported on (100)-cut GaAs propagating along the <110> direction where the total displacement at the surface of the plate is less than 10% of the maximum total displacement. The dispersion curves and the displacement component profiles show the reduction of total displacement at the surface of the plate starting when the phase velocities of the higher-order modes are crossing the shear bulk acoustic wave velocity to the value as low as 5%. Due to the concentration of acoustic energy inside the plate, the reported quasi-zero plate acoustic waves (QZ-PAW) further reduce the radiation of acoustic energy when the plate surface is in contact with liquid. The experimental results validate the occurrence of QZ-PAW with a reduction of viscous damping insertion loss compared to previously reported quasi-longitudinal Lamb waves (QL-LW). The results demonstrate the potential QZ-PAW mode for emerging applications such as dual-mode PAW sensors, PAW devices with integrated sensor and actuator, thin-film and ultra-high frequency (UHF) PAW sensors in highly viscous liquid media.

Keywords: Lamb wave, zero surface displacement, sensor, acoustics, liquid media

1. Introduction

Several types of acoustic waves (AW) devices have been extensively studied and reported for sensor application in liquid media [1]. The main aim is to prevent or minimise the radiation of acoustic energy into the liquid media. In general, AW can be classified into three different categories: bulk acoustic waves (BAW), surface acoustic waves (SAW) and plate acoustic waves (PAW). BAW-based devices with in-plane components polarisation such as Quart Crystal Microbalance (QCM) [2], lateral field excitation BAW [3], and shear mode thin-film bulk acoustic resonator (TFBAR) [4], for example, are suitable for a sensor in liquid media by having close-to-zero out-of-plane displacement component at the surface, thus preventing the conversion of acoustic energy into longitudinal pressure wave in the liquid. Similarly, several types of SAW are suitable for a sensor in liquid media, such as shear horizontal SAW (SH-SAW)[5] and Love mode (LM) [6] and high velocity pseudo-SAW (HVPSAW) [7].

The radiation of acoustic energy into the liquid can also be prevented by using the AW with phase velocity, $v_{ph,}$ lower than the compressional sound velocity of liquid media (1500 m/s in water, for instance). For PAW-based sensors in liquid media, this condition can be achieved by using the fundamental antisymmetry Lamb wave (A_0) mode [8]. However, it is limited only at a low plate thickness to wavelength ratio (h/λ), typically at an h/λ ratio lower than 0.1. Consequently, making the device very fragile or, if a thicker plate is used, a larger wavelength is necessary, thus lowering the operating frequency. Gao et al. reported the use of the mass-loading technique by using a high aspect ratio electrode to reduce the velocity of the waves lower than the velocity of the liquid with a trade-off in the reduction of electromechanical coupling coefficient and the complexity of the fabrication process to obtain high aspect ratio electrode [9].

PAW based devices have an advantage over SAW for sensor application in liquid media as they have two free surfaces that are both sensitive to surface perturbations. Thus when the interdigital transducer (IDT) is employed to convert the electrical energy into acoustic waves and vice versa in one of the surfaces, the opposite surface can be used as the sensing layer. Thus the electrical connection is separated from liquid contact without requiring an additional thin dielectric layer covering the IDT. Several types of PAW have in-plane polarisation, such as shear horizontal acoustic plate mode (SH-APM) [10] and fundamental symmetric Lamb waves (S_0) [11]. For S_0 mode, dominantly longitudinal displacement condition is also achieved at a low h/λ ratio. Therefore it has a similar limitation as A_0 mode in terms of the robustness of the device.

While AW type with in-plane polarisation minimises the acoustic energy radiation, the loss of acoustic energy is still occurring due to the penetration of in-plane particle displacement and the wave-liquid interaction length at the solid/liquid interface. Due to non-zero in-plane particle displacement at the solid surface, or even in most cases are maximum at the surface, the in-plane particle displacement exponentially decreases to zero in the liquid. The thin liquid layer in the solid/liquid, where the liquid is coupled to the oscillating surface of the plate, is called the characteristic penetration depth or a decay length δ [12] and is given by :

$$\delta = \sqrt{\frac{2\eta}{\rho\omega}} \qquad \text{Equation (1)}$$

δ is dependent on the liquid viscosity (η), liquid mass density (ρ) and the angular operating frequency (ω) of the AW. In water and for AW-based sensor with several MHz operating frequency, δ is around 50

nm. The viscous-damping insertion loss (IL) when the sensor is in contact with Newtonian liquid is given by :

$$\mathrm{IL} = \mathrm{A}\sqrt{\rho\omega\eta} \qquad \text{Equation (2)}$$

and $\mathrm{A} \approx \frac{\omega l}{\rho_s {v^2}_0}$, where l is the wave-liquid interaction length, ρ_s is the substrate mass density and the v_0 is the velocity of the wave.

As shown in equation (2), the insertion loss will increase as the liquid viscosity increases. Therefore the magnitude of insertion loss can be used to quantify the liquid viscosity. However, when the liquid viscosity is very high, the significant reduction in the signal strength affects the signal-to-noise ratio and the quality factor of the sensor, and consequently, the sensor's sensitivity. Additionally, the insertion loss will further increase when the sensor has a higher operating frequency, limiting the maximum operating frequency of the AW-based sensor application in liquid media.

In this paper, we report a type of higher-order plate acoustic wave with close-to-zero particle displacement at the surface of the plate, thus reducing the wave-liquid interaction length and the insertion loss. Finite element simulations were performed to obtain the dispersion curve, the displacement profile and the insertion loss of quasi-zero plate acoustic waves (QZ-PAW) due to viscous damping. The occurrence of QZ-PAW is validated experimentally. The performance of QZ-PAW is compared with in-plane polarised quasi-longitudinal Lamb waves (QL-LW), followed by further discussion of the potential and future application of QZ-PAW for sensor application in highly viscous liquid media.

2. Lamb Waves Theory and Finite Element Simulation

2.1 Dispersion Curves and Displacement Profile

A general solution of Lamb's characteristic equation in an isotropic and homogenous plate results in Lamb wave (LW) dispersion curves with two sets of sinusoidal waves (symmetric S and antisymmetric A modes). Lamb waves have two-component displacements: longitudinal (in-plane, u_1) and shear vertical (out-of-plane, u_3) displacements [13]. The S_0 and A_0 modes converge into Rayleigh wave (RW) velocity in a thick plate, while the higher-order modes asymptotically reach the bulk shear wave (S_{BAW}) velocity. Viktorov firstly reported the symmetric modes with dominantly u_1 displacement component, when the phase velocities of S modes reach the value of bulk longitudinal wave phase velocity (v_{SBAW}), and the u_3 vanishes on the surface of the plate [14]. These observations are further explained theoretically by Pilarsky et al. for the isotropic plate case [15]. Furthermore, Veres et al. [16] discussed the maximum and minimum of the surface displacements of LW. They reported that the longitudinal displacement component vanishes at the surface with maximal shear vertical displacement component when the LW higher-order modes phase velocity (v_{ph}) at the crossing is $v_{ph} = \sqrt{2}\, v_{SBAW}$. Thus, it is possible to obtain LW with only in-plane (QL-LW) or out-of-plane (quasi-vertical LW, QV-LW) displacement components by choosing a specific plate thickness, frequency, and wavelength.

For anisotropic and piezoelectric material, there are two solutions of S_{BAW} with two distinct v_{ph} ($S_{BAW\text{-}fast}$ and $S_{BAW\text{-}slow}$). Furthermore, when the plate is highly anisotropic (e.g. ST-cut Quartz), the solutions of the surface displacement component have a non-zero shear horizontal component (u_2). The higher-order quasi longitudinal LW (QL-LW) and quasi shear horizontal LW (QSH-LW) are reported in ST-cut

Quartz[17,18]. The higher-order modes LW with in-plane surface displacement expand the application of LW with higher frequency and higher plate thickness for a sensor in a liquid environment.

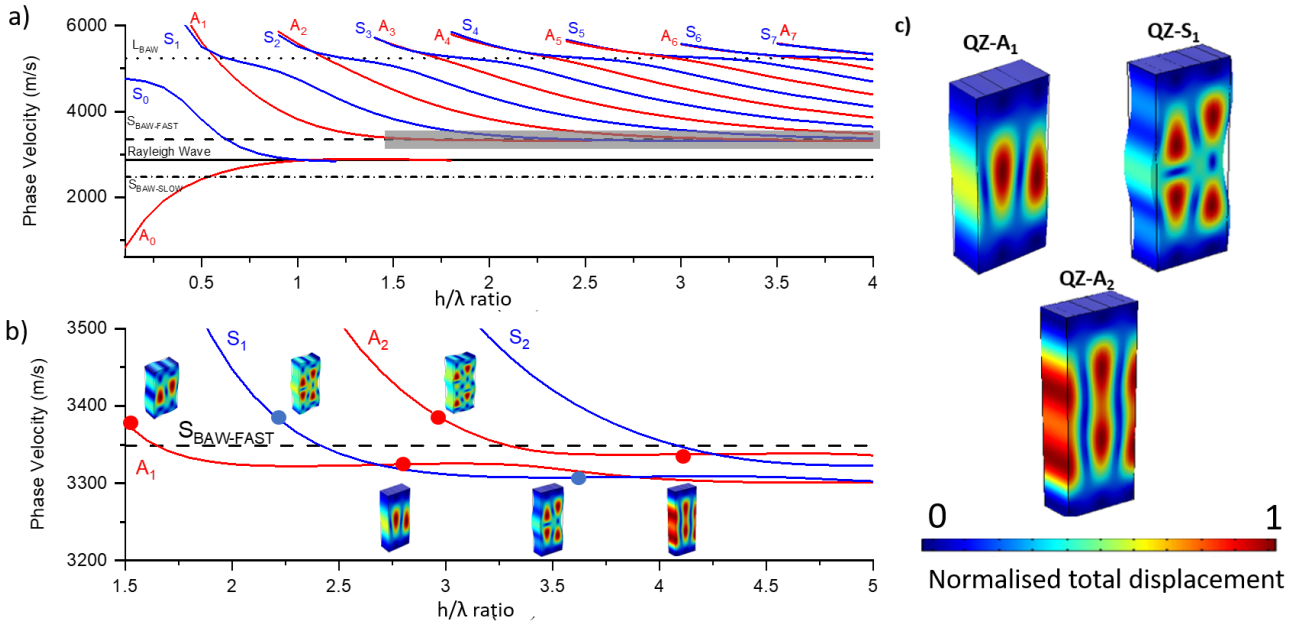

Figure 1: (a) Lamb wave dispersion curve of (100)-cut GaAs propagating along the <110>direction (b) the conversion of Lamb waves into QZ-PAW when the phase velocities of higher-order modes are lower than the fast shear BAW phase velocity, and (c) the QZ-PAW displacements of the first three higher-order modes.

3D Comsol Multiphysics eigenfrequency simulation was used to obtain the Lamb waves resonant frequencies of GaAs plate at different h/λ ratios. The solutions of eigenfrequency for each mode are multiplied by the wavelength to obtain the phase velocities (v_{ph}). Figure 1a shows the dispersion curves of the v_{ph} vs h/λ ratio of (100)-cut GaAs Lamb waves propagating on <110>-direction. GaAs is a piezoelectric material and has a cubic crystal structure. There are three v_{ph} solutions of BAW that propagates at <110> direction: one longitudinal BAW (L_{BAW}) and two S_{BAW}. The BAW phase velocities are 5240 m/s, 3345 m/s and 2475 m/s for L_{BAW}, $S_{BAW\text{-}fast}$ and $S_{BAW\text{-}slow}$ respectively [19]. The solution of $S_{BAW\text{-}slow}$ v_{ph} is lower than the RW v_{ph}. The particle displacement is out-of-plane for $S_{BAW\text{-}fast}$ (shear vertical) and in-plane for $S_{BAW\text{-}slow}$ (shear horizontal). As shown in figure 1a, the A_0 and S_0 modes v_{ph} converge into RW.

Figure 1b shows the inset where the higher-order modes are converging into the v_{ph} of $S_{BAW\text{-}fast}$. As shown in figure 1b, at a higher h/λ ratio, the modes are crossing the v_{ph} of $S_{BAW\text{-}fast}$ and then stagnating with a slight fluctuation slightly below the $S_{BAW\text{-}fast}$ v_{ph}, which is different from the expected behaviour of higher-order modes based on Lamb waves characteristic equation in the case of isotropic plate material. In supplementary material 1 (S1), using the same COMSOL FEM method, the dispersion curves of A_1 and S_1 modes for (100)-cut GaAs propagation along <110> with an isotropic GaAs by assuming it has only two independent variables ((C_{11}, C_{12}, and $C_{44} = (C_{11}\text{-}C_{12})/2$) are plotted to compare the different behaviour of isotropic and anisotropic plate.

For the isotropic case, The A_1 and S_1 modes are asymptotically reaching the S_{BAW} velocity at a higher h/λ ratio, which agrees with the solution of the LW characteristic equation. However, for anisotropic material, even for the simplest cubic crystal structure with three independent variables, the equations will become more complex, resulting in different behaviour of dispersion curves. In material with a higher degree of anisotropic such as ST-cut Quartz, the higher-order modes are lowly dispersive around the $S_{BAW-FAST}$ before the v_{ph} values drop asymptotically, reaching the value of $S_{BAW-SLOW}$ [18]. The values of $S_{BAW-FAST}$ (5100 m/s) and $S_{BAW-SLOW}$ (3298 m/s) are higher than the RW (3157 m/s) in ST-cut Quartz. Furthermore, the piezoelectricity effect will also affect the behaviour of the dispersion curves

In addition to the fluctuating value of v_{ph} slightly lower than the $S_{BAW-FAST}$, the total displacement at the surface of the plate (u_{surf}) of the higher-order modes is reducing relative to the maximum total displacement inside the plate (u_{max}). The QZ-PAW for the first three higher-order modes (A_1, S_1 and A_2) are shown in figure 1c. As shown in figure 1c, the particle displacement and the acoustic energy are concentrated inside the plate with almost zero total displacement values at the surfaces.

Figure 2a shows the total displacement on the plate surface normalised by the maximum total displacement inside the plate (u_{surf}/u_{max}) vs the h/λ ratio for the first four higher-order modes. As shown in figure 2a, the u_{surf}/u_{max} reduces to the value as low as 5% at h/λ ratio of 2.3 to 3.1, 3.5 to 4.8, and 3.8 to 4.7 for A_1, S_1 and A_2 modes, respectively. Referencing the definition of QL-LW mode in [18], here we define the quasi-zero plate acoustic waves (QZ-PAW) as the LW with the u_{surf}/u_{max} equal to 10% or less. By this definition, the range of h/λ ratio for QZ-PAW is 2.1 to 3.3, 3.3 to 4.5 and 3.7 to 4.8 for A_1, S_1 and A_2 modes, respectively.

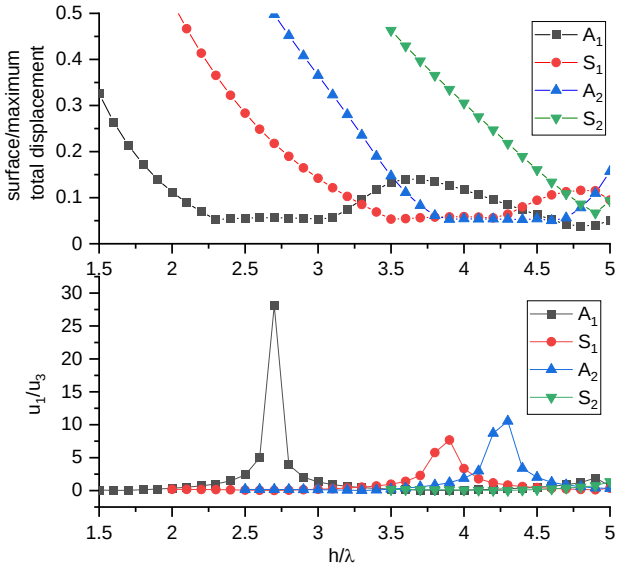

Figure 2: The ratio between (a) total displacement at the surface of the plate and the maximum displacement inside the plate (u_{surf}/u_{max}) and (b) Longitudinal and shear vertical (u_1/u_3) at the surface of the plate

The total displacement is the sum of u_1, u_2, and u_3 particle displacement components. The u_1 and u_2 are in-plane particle displacements, while u_3 is out-of-plane displacement. In this case, due to the cubic crystal symmetry, u_2 is zero. Thus only u_1 and u_3 are contributing to the total displacement. Figure 2b shows the

ratio of u_1/u_3 at the surface of the plate. As shown in figure 2b, for A_1 mode, the surface displacement is dominantly in-plane longitudinally polarised at the h/λ ratio of 2.7. Similarly, for S_1 and A_2 modes, the h/λ ratios with dominantly longitudinal displacement are 3.9 and 4.3. Thus, while the u_{surf}/u_{max} at different h/λ ratios are almost the same (5% for A_1 mode at h/λ from 2.3 to 3.1, for instance), the u_1/u_3 are significantly different, which will affect the magnitude of insertion loss when the plate will be in contact with liquid.

In figure 2a, the u_{surf}/u_{max} of A_1 mode is higher than 10% at the h/λ ratio of 3.4 to 4.2 and reducing again to lower than 10% at the h/λ ratio of 4.3 and higher, indicating a periodicity in u_{surf}/u_{max} with respect to the h/λ ratio. Similar periodic behaviour is also shown in the fluctuation of v_{ph} when the value is lower than $v_{BAW\text{-}FAST}$. The u_{surf}/u_{max} is plotted with the $v_{ph}/v_{BAW\text{-}FAST}$ for A_1 and S_1 modes in figures 3a and 3b, respectively. As shown in figure 3, the lower value of u_{surf}/u_{max} correlates to the less dispersive region when the v_{ph} is almost constant to the change in the h/λ ratio. Conversely, when the wave is becoming more dispersive, the u_{surf}/u_{max} increases. This correlation shows that the condition of the QZ-PAW is achieved when the wave is less dispersive. Furthermore, the fluctuation in both $v_{ph}/v_{BAW\text{-}FAST}$ and u_{surf}/u_{max} ratio shows that higher-order modes remain dispersive at higher plate thickness. In contrast, the fundamental modes A_0 and S_0 are converted into a non-dispersive RW with a constant phase velocity value.

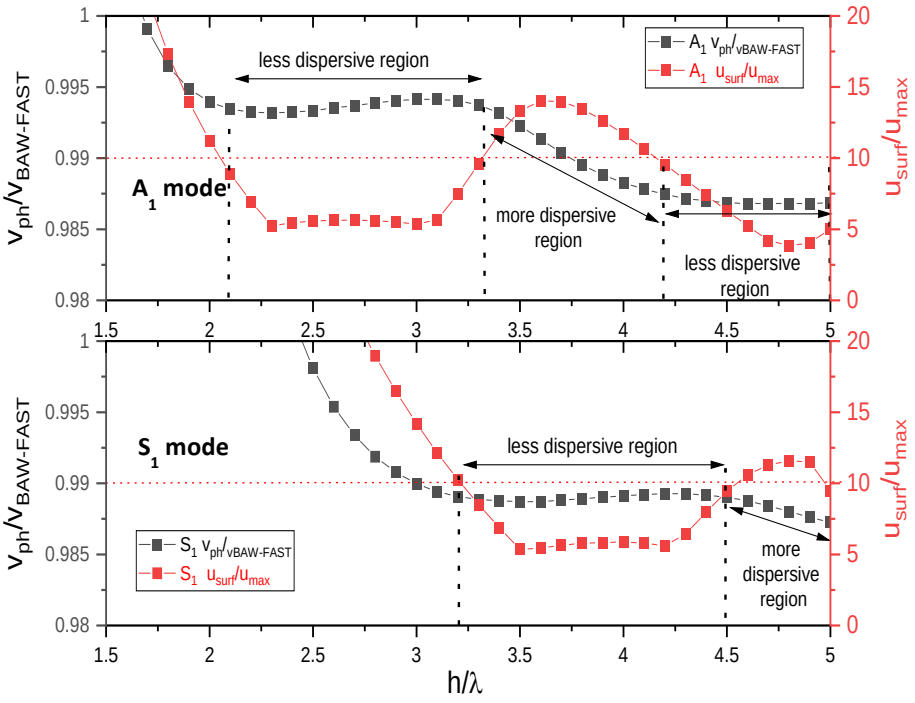

Figure 3: The correlation in the fluctuation of $v_{ph}/v_{BAW\text{-}FAST}$ and u_{surf}/u_{max} of (a) A1 mode and (b) S1 mode

Figure 4 shows the normalised displacement components profiles of A_1, S_1 and A_2 modes at h/λ ratio of 2.7, 3.9 and 4.3, respectively. As shown in figure 4, the u_3 for the three modes vanishes at the surface. The particle displacement at the surface is dominantly longitudinal with the normalised displacement amplitude of only 5% of the maximum displacement inside the plate. A small in-plane displacement on

the surface of the plate in contact with the liquid will reduce the wave-liquid interaction length, thus reducing the insertion loss as given in equation (2). Therefore, they are expected to have the least acoustic energy radiation to the surrounding media and the minimum insertion loss due to viscous damping.

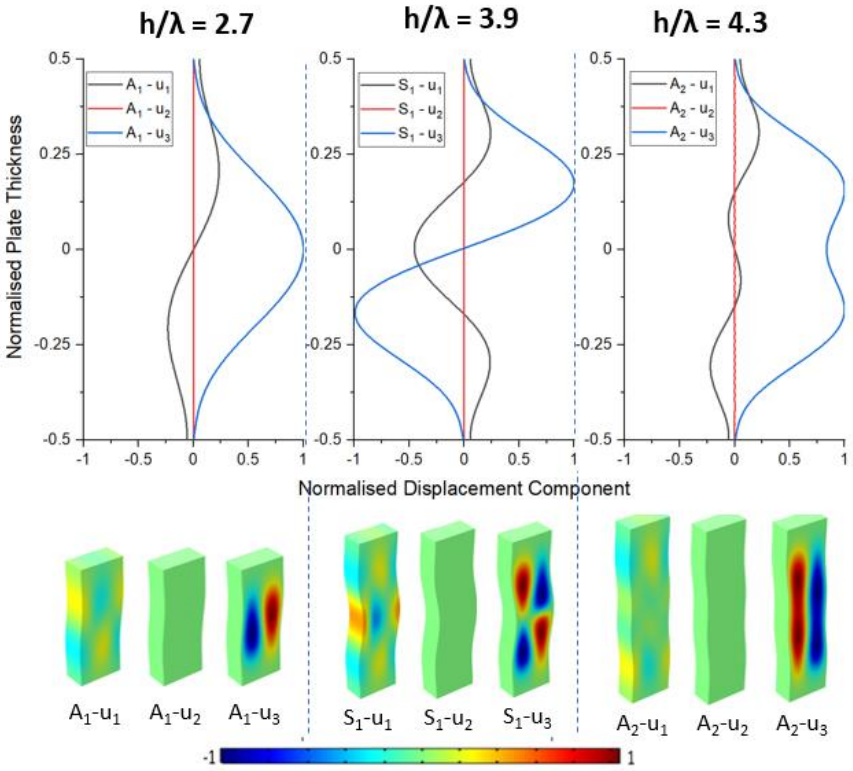

Figure 4: Particle displacement components profile of the first three QZ-PAW at h/λ ratio of 2.7 (A_1), 3.9 (S_1) and 4.3 (A_2)

2.2 Electromechanical Coupling Coefficients

A general limitation of higher-order modes is the reduction of the electromechanical coupling coefficient (K^2) when a thicker plate or a higher-order number is used [20]. Furthermore, since the conversion of electrical to acoustic energy occurs at the surface where the IDT is located, it is expected that the QZ-PAW will have an even smaller K^2. The deposition of the metal layer at the opposite surface of the IDT changes the electrical boundary condition and can potentially increase the value of K^2 [20,21]. Figures 5a and b show the K^2 of A_1, S_1, A_2 and S_2 modes with Plate-IDT (S-IDT) and Metal-Plate-IDT (M-P-IDT) coupling configuration, respectively, vs the h/λ ratio at the range where QZ-PAWs exist. As shown in figure 5a and 5b, the K^2 value reduces with the minimum K^2 at h/λ ratio of 2.9, 4 and 4.5 for A_1, S_1 and A_2 modes, respectively.

Comparing the lowest K^2 for each mode to the higher u_1/u_3 at h/λ ratio, we can observe a shift of around 0.1 to 0.2 h/λ ratio. The h/λ ratios for the modes with the highest longitudinal component (u_1/u_3 ratio) do not correspond to the h/λ ratios with the lowest K^2. The correlation of K^2 to u_{surf}/u_{max} does not explain the lowest K^2 at a specific h/λ ratio. For A_1 mode, for instance, the lowest K^2 is at h/λ ratio of 2.9, while the u_{surf}/u_{max} ratios are almost constant, around 5% for the h/λ ratio range from 2.3 to 3.1. One possible reason we cannot observe a direct correlation is that the K^2 value is affected by more complex interaction between

both longitudinal and shear horizontal components to the piezoelectricity coupling coefficient. At h/λ ratio when the QZ-PAW is dominantly longitudinal, the K^2 is in the order of between 10^{-5} to 10^{-6}. Furthermore, adding a metal layer for M-P-IDT configuration, as shown in figure 5b, does not improve the K^2.

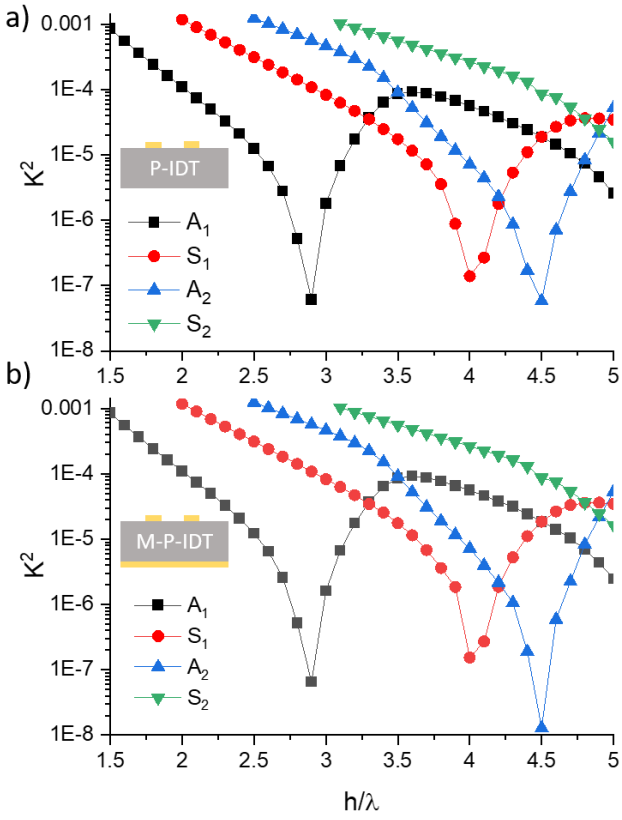

Figure 5: K^2 for (a) P-IDT and (b) M-P-IDT configuration

The K^2 is related to the conversion rate of electrical energy into acoustic energy and vice versa. For instance, for two-port delay line device implementation, the value of K^2 will affect the power received in the receiver IDT. Based on the K^2 values, we can expect the S_{21} transmission signal strength will be in the range of -50 dB to -60 dB. While the S_{21} signals will be relatively low, however level of the signal floor is more important in practical application. The signal floor is highly affected by the feedthrough of electromagnetic waves that instantaneously transmit the electrical power from the transmitter to receiver IDT. One of the methods to reduce this feedthrough is by electrically grounding the wafer's backside, thus preventing the feedthrough effect due to the substrate conductivity. This method can reduce the signal floor by 10 to -15 dB [22]. While the addition of the metal at the back of the substrate does not improve the K^2, it can reduce the signal floor in the S_{21} scattering transmission parameter by electrically grounding the metal layer.

2.3 Solid/Liquid Contact Insertion Loss

3D COMSOL Multiphysics eigenfrequency simulations were performed to calculate insertion loss when one of the plate surfaces is in contact with liquid. We used the isotropic viscoelastic material model for the liquid domain to be able to consider both shear (η_v) and bulk viscosity (η_b) of the liquid [23], with

more detail in the simulation model described in supplementary material 2 (S2). The value of η_v and η_b are 0.00093 Pa.s and 0.0023 Pa.s. Figure 6a shows the total displacement profile of QZ-PAW A_1, S_1 and A_2 modes at h/λ ratios of 2.7, 3.9 and 4.3, respectively. As shown in figure 6a, the total displacement and acoustic energy are concentrated inside the plate and close to zero at the plate/liquid interface. The complex resonant frequencies were obtained from the simulation, and the complex phase velocities ($v_{ph} = v_r + jv_{i)}$ were obtained by multiplying the resonance frequency with the wavelength. The imaginary part of the phase velocities indicates a leaky Lamb wave where some of the acoustic energies are radiated into the liquid. Higher radiation of acoustic energy will be translated into a higher insertion loss (IL) value in dB/λ, which can be calculated by the equation below [24]

$$IL = -40\pi(log_{10}e)\frac{v_i}{v_r} = -54.6\ \frac{v_i}{v_r} \qquad \text{(Equation 3)}$$

The theoretical insertion losses vs the h/λ ratios are plotted in figure 6b for the first four higher-order LW modes, in contact with DI water and propagating at a distance of 250 λ. The wavelength of the LW devices in this simulation is 168 μm, so the propagation distance is equal to 42mm. As shown in figure 6b, the ILs is less than 1 dB for the h/λ range of QZ-PAW when the surface displacement is less than 10% of the maximum displacement inside the plate. The lowest losses, as expected, are achieved at the h/λ ratios of 2.7, 3.9 and 4.3 for A_1, S_1, and A_2 modes, respectively, when the surface displacement components are dominantly longitudinal and u_{surf}/u_{max} of around 5%.

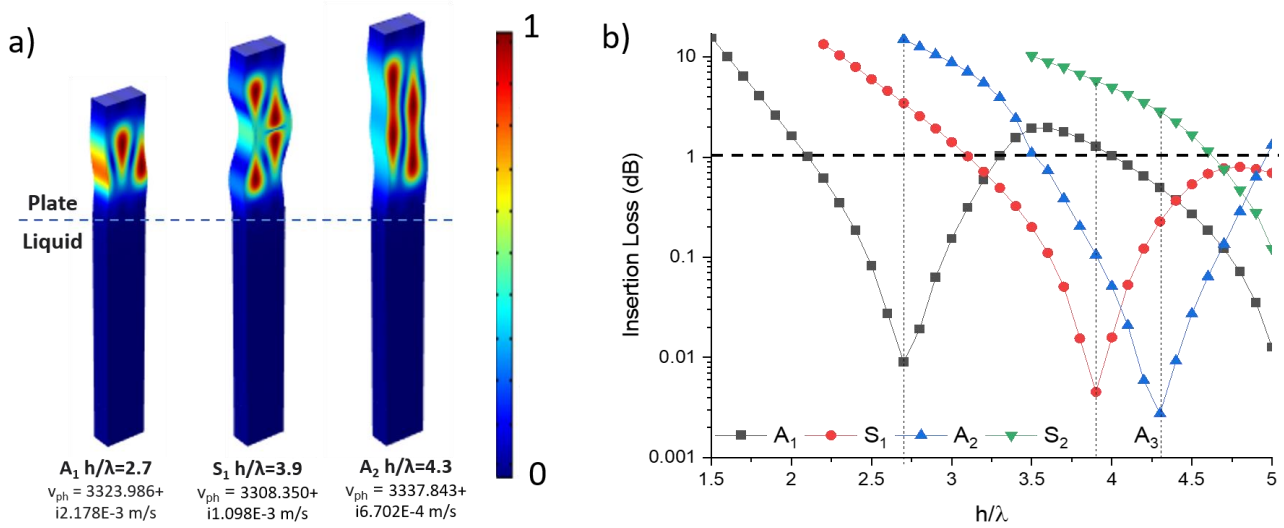

Figure 6: (a) Total displacement profile of QZ-PAW in contact with liquid and (b) Insertion loss of the A_1, S_1, A_2 and S_2 modes in dB for the waves travelling at the distance of 250λ

The lowest theoretical ILs are 0.00894 dB for A_1 mode, 0.00453 for S_1 mode and 0.00274 for A_2 mode. However, at the h/λ ratios with the lowest IL, several other modes have a very close phase velocity and resonant frequency. For example, at h/λ of 2.7, the A_1 and S_1 modes have resonant frequencies of 19.786 and 19.78 MHz, respectively. Thus the difference between the resonance peak is merely 6kHz. While A_1 is a QZ-PAW with the lowest theoretical IL, S_1 mode is not a QZ-PAW with u_{surf}/u_{max} of 22% and the

theoretical IL of 3.45. Therefore, the resonant bandwidth must be less than 6 kHz to separate the resonant peaks for A_1 and S_1 modes in the frequency response signal. This bandwidth value will be challenging to achieve, especially in the two-port delay line device implementation. The summary of the non-QZ modes merged into the QZ-PAW modes is summarised in Table 1. As shown in Table 1, a challenge of the multiple modes merging into a single peak also similarly occurs in h/λ ratio of 3.9 and 4.3, limiting the minimum insertion loss for the practical applications of the device.

Table 1: List of the merged LW higher-order modes with QZ-PAW resonant peak h/λ of 2.7, 3.9 and 4.3

h/λ	Modes	Freq (MHz)	u_{surf}/u_{max} (%)	IL (dB)	Types
2.7	A_1	19.786	5.6	0.00894	QZ
	S_1	19.78	22	3.45	non-QZ
3.9	A_1	19.692	13	1.27	non-QZ
	S_1	19.695	5.8	0.00453	QZ
	A_2	19.865	5.9	0.106	QZ
	S_2	20.033	33	5.78	non-QZ
4.3	A_1	19.661	8.5	0.495	QZ
	S_1	19.702	6.4	0.228	QZ
	A_2	19.871	5.3	0.00274	QZ
	S_2	19.859	22	2.85	non-QZ
	A_3	20.292	45	7.80	non-QZ

2.4 Time Domain Simulation

Two-port delay line QZ-PAW devices were simulated using COMSOL Multiphysics time-domain study to obtain the S_{21} frequency response of the devices. From the 3D model, the u_2 is always zero across the plate. Therefore to simplify the simulation, a 2D model of a two-port delay line will be sufficient to obtain a relatively accurate simulation result. An impulse response of 1 ns is applied in the transmitter IDT to excite the Lamb wave modes. The waves are propagating across the plate, and the output voltage signals at the receiver IDT were recorded. The IDTs wavelength is 168 μm, and the IDTs have 50 finger pairs with a delay length of 200λ, thus equal to the IDT centre to centre distance of 250λ. The signal's bandwidth can be approximated by dividing the resonance frequency by the number of IDT finger pairs. Thus for the QZ-PAW resonance peak of around 19.7 MHz, the bandwidth will be around 394 kHz. The output signals are converted into the frequency domain by Fourier transform, and the S_{21} transmission scattering parameter is calculated from the ratio of output and input voltage with the equation below :

$$S_{21}\ (\text{dB}) = 20 \log (V_{out}/V_{in}) \qquad \text{(Equation 4)}$$

The simulated S_{21} scattering parameter frequency response at the h/λ ratios of 2.7, 3.9, and 4.3 is shown in figures 7a, 7b and 7c, respectively. As shown in figure 7a, the A_1 and S_1 modes are merged into a single resonant peak. Similar conditions are also shown in figures 7b and 7c for h/λ 3.9 and 4.3, respectively. In figure 7b, at 3.9 h/λ ratio, the A_1 mode is no longer classified as QZ-PAW with u_{surf}/u_{max} value of 13%. However, since the total displacement at the surface is still relatively low, the theoretical insertion loss in DI water liquid contact is reasonably low at 1.27 dB. The main challenge is to separate the S_2 mode with

u_{surf}/u_{max} value of 33% and the insertion loss of 5.78 dB. The resonant frequency difference between A_2 and S_2 modes is 170 kHz. In figure 7c, at h/λ ratio of 4.3, both S_2 and A_3 modes are non-QZ-PAW modes with resonant frequency differences from A_2 mode of 12 kHz and 421 kHz, respectively.

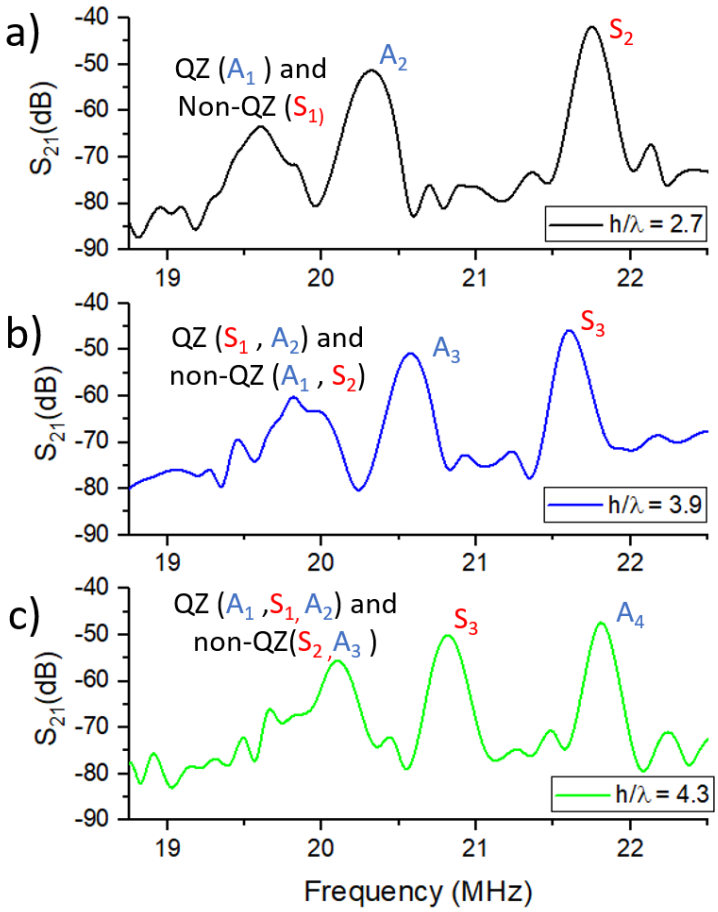

Figure 7 Simulation results of S_{21} transmission scattering parameter for GaAs two-port delay line device with h/λ of (a) 2.7, (b) 3.9 and (c) 4.3

A_2 and S_2 modes resonant peaks distance can be increased by using h/λ ratio lower than 3.9 to increase the S_2 v_{ph}. For example, as shown in Table 2, when the h/λ ratio is reduced to 3.7, the difference between A_2 and S_2 modes is increased from 170 kHz to 319 kHz to separate the resonance peaks, with a trade-off in the increase of with u_{surf}/u_{max} and insertion loss of A_1 mode to 14% and 1.79 dB. Another advantage of using the h/λ ratio of 3.7 is to obtain the QL S_6 mode with a dominantly longitudinal displacement [20], to compare the insertion loss between QZ-PAW and QL-LW, which will be demonstrated in the experimental results.

Table 2 List of the merged modes with QZ-PAW resonant peaks at h/λ = 3.7

h/λ	Modes	Freq (MHz)	u_{surf}/u_{max} (%)	IL (dB)	Types
3.7	A_1	19.739	14	1.79	non-QZ
	S_1	19.704	5.6	0.0510	QZ
	A_2	19.878	8.3	0.385	QZ

	S_2	20.197	40	7.89	non-QZ

3. Experimental Validation and Discussion

To validate the occurrence of QZ-PAW experimentally, we designed a two-port delay line devices using a standard 3-inch (100)-cut GaAs wafers with thicknesses of 625 µm and 650 µm, with the main hypothesis in the reduction of insertion loss when the surface of the plate is in contact with liquid. The IDT designs are identical for both wafers with a wavelength of 168 µm. Thus the h/λ ratios are 3.7 and 3.9 for the 625 µm and 650 µm wafers, respectively. The IDTs have 50 finger pairs with an aperture of 50λ. The delay line length is 200λ so that the centre to centre distance between the transmitter and receiver IDTs is 250λ or equal to 42 mm. The direction of propagation is parallel to the wafer flat, which corresponds to <110> direction. The Piranha process cleaned the GaAs to remove organic contamination, followed by dehydration baking. For IDTs patterning, the wafer was coated by Ti prime as a photoresist adhesion layer and negative photoresist of nLOF AZ2000. The thickness of the photoresist is 1.3 µm. The wafer was exposed using EVG 6200 photolithography tools followed by photoresist hardbake and development process. 100 nm of aluminium is used as an electrode with 10 nm Cr as an adhesion layer, and they were deposited by the electron beam evaporator. After metal deposition, the photoresist was stripped using photoresist remover for the lift-off process. 50nm Au was deposited at the back of the wafer to obtain an M-P-IDT coupling configuration. Even though the M-P-IDT configuration does not improve the K^2, the electrically short boundary condition at the sensing layer will reduce the electromagnetic feedthrough [22] and decouple liquid conductivity [25]. The wafers were attached to PCB with a centre hole so that the IDTs and the delay line are on the wafer that is suspended to obtain free surfaces mechanical boundary condition. The backside of the wafer is electrically connected to the ground of the PCB to obtain an electrically grounded boundary condition. The image of the fabricated devices on the PCB and the experimental set-up can be found in supplementary material 3 (S3).

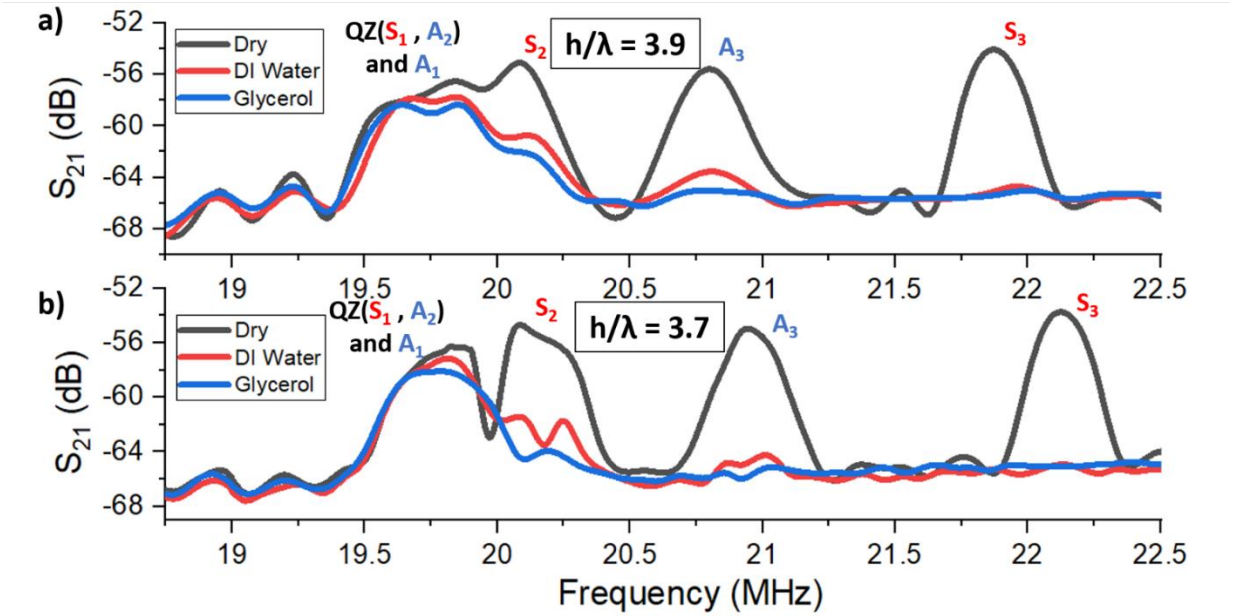

Figure 8. S_{21} scattering parameter vs frequency experimental results of Lamb waves two-port delay line device with h/λ of (a) 3.9 and (b) 3.7

Figure 8 shows the characterisation results of two two-port delay line devices having an h/λ ratio of 3.9 and 3.7 in figures 8a and 8b, respectively, with and without liquid contact. DI water and 100% glycerol were used as liquid contact. Despite the low K^2 value, the signal resonant peaks of around -56 dB are observable from the signal floor of -68 dB. As shown in figure 8a, at 3.9 h/λ, A_1, S_1, A_2 and S_2 modes are combined into a single peak, as previously predicted in the time domain simulation results. The first resonant peak in figure 8a has a large bandwidth due to a merge of four waves with theoretical frequency ranges from 19.692 MHz to 20.033 MHz. However, since the S_2 mode has a total surface displacement of 33 % and theoretical IL of 5.78 dB, the S_2 mode will have a much higher insertion loss when the plate is in contact with liquid. As shown in figure 8a, the reduction in S_{21} is asymmetrical with around 6 dB reduction in the frequency area higher than 20 MHz, which corresponds to the S_2 mode. Thus, the significant reduction in the S_2 mode separates the S_2 mode from the other three modes with lower resonance frequencies.

The A_1 mode has a relatively higher theoretical insertion loss of 1.27 dB than the S_1 and A_2 modes, with theoretical insertion losses of 0.005 and 0.1 dB. As the reduction in S_{21} is around 1 dB in the frequency area lower than 20 MHz, it could be expected that the A_1 mode contributes to the reduction in the S_{21} signal and the remaining S_{21} peak observed when the surface in contact with DI water consists of the QZ-PAW modes of S_1 and A_2. Hence, while the four modes merged into a single peak in a dry environment, higher S_{21} signal reduction in the liquid media will filter out the non-QZ mode from the QZ-PAW resonant peak. Furthermore, when the liquid contact is replaced from DI water to glycerol with much higher viscosity, there is a further reduction of around 0.8 dB in the resonance peak of the QZ mode. Additionally, as shown in figure 8a, the A_3 and S_3 modes are fully damped with liquid contact. The signal is fully damped because both modes have a maximum displacement at the surface with out-of-plane u_3 components. Consequently, acoustic energy is fully radiated into the liquid and is not received in the receiving IDT.

For practical applications of sensor devices in quantitatively monitoring physical parameters of the liquids, it is necessary to separate the S_2 mode without the liquid contact so that the QZ-mode signal peak and the bandwidth can be identified and calculated. For separating the S_2 mode peak from the lower frequency peak, a thinner GaAs wafer with a thickness of 625 μm was used to lower the h/λ. At 3.7 h/λ, the v_{ph} is higher, thus increasing the difference in the resonant frequency peak between S_2 and A_2 modes. As shown in Figure 8b, the S_2 mode is further separated from the other three modes as the theoretical resonant frequency difference increases from 170 kHz to 319 kHz.

However, the resonance frequency difference of 319 kHz is still lower than the signal bandwidth of 394 kHz, thus meaning that the S_2 mode is not completely separated, which can be the reason for the appearance of two peaks below the S2 mode label in figure 8b. The frequency difference can be further increased by a lower h/λ ratio of 3.6, with the trade-off in higher surface displacement and higher insertion loss. Despite this limitation, the reduction in IL when the surface is in contact with liquid can be qualitatively calculated in QZ-PAW with 3.7 h/λ. Furthermore, at the h/λ ratio of 3.7, the GaAs device will also excite the S_6 mode with dominantly longitudinal displacement at the surface (QL-S_6 mode) with the v_{ph} close to LBAW v_{ph} [20]. The detail on the QL-6 mode is described in supplementary material 4 (S4). Thus it will be possible to compare the performance of QZ-PAW mode with QL-LW mode when the surface is in contact with highly viscous liquid. Figures 9a and 9b compare the QZ-PAW mode and QL-LW mode in dry and liquid contact. The QL-LW has a higher v_{ph}, thus a higher resonant frequency. As shown in figure 9a, the QZ-PAW mode has 1.8 dB reduction in S_{21} from dry to glycerol contact, about one-third of the S_{21} reduction of QL-LW mode. The loss of 5.1 dB of the S_6 QL-LW mode, as shown in

figure 9b, is comparable with the previously reported S_1 QL-LW mode in ST-cut quartz with a similar operating frequency [26].

Figure 9c shows the change in the insertion loss when the plate surface is in contact with different DI water/glycerol mixtures, with the insertion loss in DI water as the reference value. The concentration of glycerol is 25%, 50%, 75% and 100%. The viscosity and mass density increase as the increase of glycerol concentrations and the change in insertion loss is plotted against the square root of the mass density and viscosity product. As shown in figure 8c, using the DI water as a reference, the change in the insertion loss is 0.95 dB when 100% glycerol is used for QZ-PAW and 3.9 dB for QL-LW. Thus the QL-LW has almost four times higher insertion loss. The saturation of insertion loss at higher viscosity is similar to the previously reported viscosity sensor based on SH-APM mode [12]. The result shows the advantage of the QZ-PAW mode in further reducing acoustic energy radiation due to lower total displacement at the surface, which reduces the wave-liquid interaction length, and consequently, the insertion loss due to viscous damping.

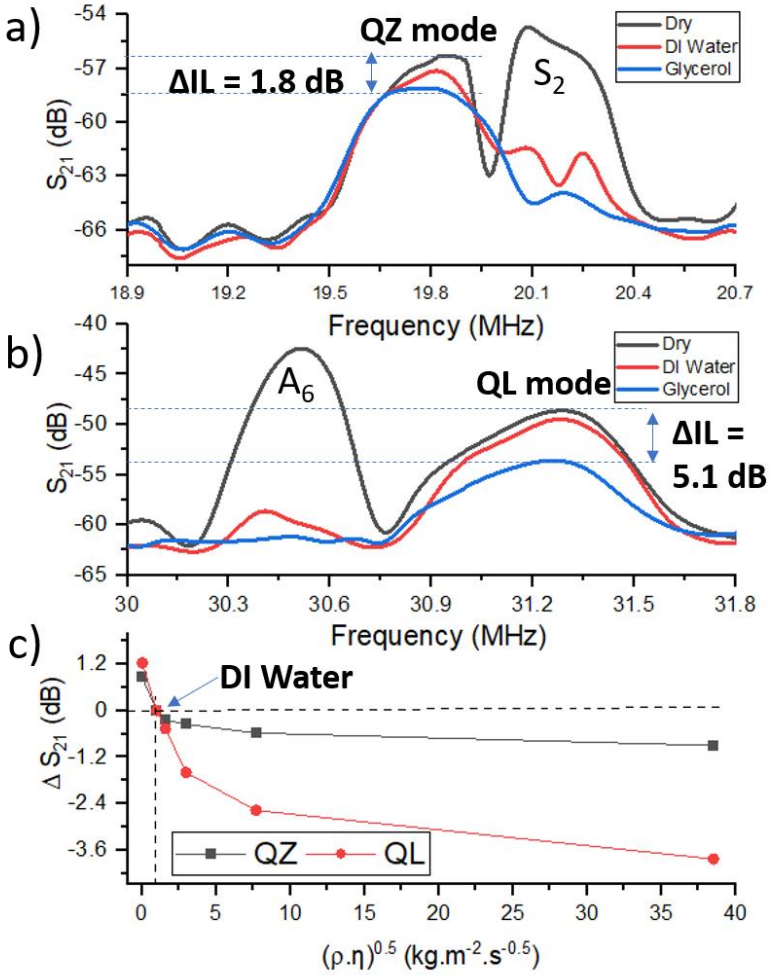

Figure 9 Insertion loss comparison (a) QZ mode and (b) QL mode in contact with DI water and glycerol, and (c) the change in S_{21} insertion loss at different concentrations of DI Water/glycerol mixture

The sensor signals (phase velocity, frequency, or attenuation) are highly affected by the surface condition. Since the QZ-PAW modes are not sensitive to surface perturbation, thus they are not suitable for the sensing mechanism based on surface perturbation principle as liquid viscosity or mass sensors,

which is the main disadvantage of QZ-PAW for sensor application. For example, QZ-PAW will have lower sensitivity but a wider dynamic range for highly viscous media than QL-LW for viscosity sensors. Furthermore, QZ-PAW can be used for a physical sensor that affects the elasticity constant of the whole plate, such as temperature, strain and pressure sensor [27,28].

This advantage is especially beneficial for sensor application in highly viscous media as it will prevent a significant reduction in signal strength due to viscous damping. Additionally, for guided acoustic waves with maximum displacement at the surface, the surface roughness is one of the leading causes of signal attenuation in [29], especially for the modes with out-of-plane displacement, due to acoustic energy scattering at the surface as the wave propagating. With QZ-PAW, this problem can be prevented and will be beneficial when the plate is thinned down by a micromachining process such as dry etching, which will introduce roughness at the surface of the plate.

Despite several advantages of QZ-PAW, there are still several challenges to be addressed to utilise the QZ-PAW in practical application. First, while the signal resonant peaks of around -56 dB are observable from the signal floor of -68 dB, it is important to improve the signal to noise ratio by increasing the signal strength. In this case, the weak signal is directly related to the low value of K^2. There are two possible methods in improving the K^2 related to the piezoelectric materials. First, due to weak piezoelectricity in a cubic GaAs plate, a thin-film piezoelectric layer such as ZnO can be deposited on GaAs for piezoelectric field enhancement and signal strength improvement in RW [30] and LW [31] devices. However, the deposition of the thin film will also affect the displacement component profile across the plate, which may increase the displacement on the surface of the plate. Thus, it is necessary to find the optimum thin-film thickness to improve the signal strength while keeping the surface displacement lower than 10% of maximum displacement inside the plate. Another possible improvement is replacing the GaAs plate with another piezoelectric material with a more complex crystal structure and higher piezoelectricity. Similarly, future study is required to verify the occurrence of QZ-PAW in piezoelectric material with different crystal structures, crystal cut and direction of propagation.

Furthermore, as different modes types with different displacement profiles can be excited in the same device with the same IDT, dual-mode PAW sensors can be implemented to decouple physical parameters such as density and viscosity [32] or pressure and temperature [33], utilising different behaviours of QL-LW and QZ-PAW in response to different physical parameters. Furthermore, the out-of-plane mode can be utilised for liquid actuation, thus integrating the liquid sensor and actuator functions within the same device [34]. Finally, the sensor sensitivity is proportional to the operating frequency; a sensor with GHz operating frequency is needed to obtain a high precision sensor and reduce the limit of detection [35]. However, for current state-of-the-art AW-based sensors, the GHz operating frequency in liquid media is impractical due to too high insertion loss.

QZ-PAW modes can potentially solve the limitation of AW-based GHz sensor devices in a liquid environment, especially when individual QZ-PAW mode resonant peaks can be separated to achieve the lowest theoretical insertion loss. However, as previously shown in the experimental result, separation of an individual peak in multi-mode devices remains a challenge, which may require the trade-off between the minimum practical insertion loss and the separation of individual modes. To solve this challenge, the improvement could be achieved by designing QZ-PAW devices with lower bandwidth using a higher number of IDTs or by exploring different piezoelectric materials, crystal cuts, and propagation directions.

4. Conclusion

We presented a higher-order Lamb wave type with a quasi-zero surface displacement component on a GaAs piezoelectric plate. We defined the quasi-zero plate acoustic waves (QZ-PAW) modes as the higher-order Lamb waves modes with the concentration of acoustic energy inside the plate and the total surface displacement of less than 10% relative to the maximum total displacement inside the plate. We performed finite element simulation using COMSOL Multiphysics software to calculate the h/λ range and the theoretical insertion loss of QZ-A_1, QZ-S_2, and QZ-A_3 modes when the surface of the plate is in contact with liquid. Despite several challenges in the practical implementation of QZ-PAW devices, we demonstrate experimentally the two-port delay line devices utilising QZ-PAW modes. Furthermore, the improvement in the insertion loss in highly viscous liquid is shown compared to QL-LW modes. Finally, we discussed the potential application of QZ-PAW to answer some challenges in the future emerging application of AW-based sensors such as dual-mode sensors and UHF sensors in highly viscous media.

Acknowledgements

This journal publication is part of the SmOoC project that has received funding from the European Union's Horizon 2020 research and innovation programme under the Marie Skłodowska-Curie grant agreement No. 844135. The work was partly supported by the French Renatech network and its FEMTO-ST technological facility

References

[1] Caliendo C and Hamidullah M 2019 *J. Phys. D: Appl. Phys.* **52** 153001
[2] Auge J, Hauptmann P, Hartmann J, Rösler S and Lucklum R 1995 *Sensors and Actuators B: Chemical* **24** 43
[3] Bienaime A, Liu L, Elie-Caille C and Leblois T 2012 *The European Physical Journal-Applied Physics* **57** 21003
[4] Wingqvist G, Bjurström J, Liljeholm L, Yantchev V and Katardjiev I *Sensors and Actuators B: Chemical* **123** 466
[5] Kondoh J 2013 Electron. Commun. **96** 41
[6] Gizeli E, Goddard N J, Lowe C R and Stevenson A C 1992 *Sensors and Actuators B: Chemical* **6** 131
[7] Tong X and Zhang D 1999 *Sensors and Actuators A: Physical* **78** 16.
[8] Zhu Z and Wu J 1995 *The Journal of the Acoustical Society of America* **98** 1057.
[9] Gao F, Al-Qahtani A M, Khelif A, Boussaid F, Benchabane S, Cheng Y, El Agnaf O and Bermak A 2020 *IEEE Sensors Journal* **21** 2725
[10] and Martin S J, Ricco A J, Niemczyk T M and Frye G C 1989 *Sensors and actuators* **20** 253
[11] Zhou L, Wu Y, Xuan M, Manceau J F and Bastien F 2012 *Sensors* **12** 10369-10380.
[12] Ricco, A.J. and Martin, S.J., 1987 *Applied Physics Letters* **50** 1474
[13] Lamb H 1917 *Proceedings of the Royal Society of London. Series A, Containing papers of a mathematical and physical character*
[14] Viktorov I A 1967 *Rayleigh and Lamb Waves: Physical Theory and Application* (New York: Plenum Press)
[15] Pilarski A, Ditri J J and Rose J L 1993 *The Journal of the Acoustical Society of America* **93** 2228
[16] Veres I A, Berer T, Grünsteidl C and Burgholzer P 2014 *Ultrasonics*, **54** 759
[17] Anisimkin VI 2013 *IEEE transactions on ultrasonics, ferroelectrics, and frequency control* **60** 2204
[18] Gulyaev Y V 2007 *IEEE transactions on ultrasonics, ferroelectrics, and frequency control* **54** 1382
[19] Bateman T B, McSkimin H J, and Whelan J M 1959 *Journal of Applied Physics* **30** 544
[20] Hamidullah M, Rezzag N, Élie-Caille C and Leblois T 2021 In *2021 IEEE Sensors Proceeding* (accepted) arXiv:2107.13677
[21] Zou J, Lin C M, Lam C S Pisano A P 2017 *Journal of Applied Physics* **121** 154502
[22] Visser J H and Venema A 1988 In *IEEE 1988 Ultrasonics Symposium Proceedings*
[23] Mirea T and Yantchev V 2015 *Sensors and Actuators B: Chemical* **208** 212
[24] Liu J 2014 Aip Advances **4** 077102.
[25] Anisimkin V I, Caliendo C, and Verona E 2016 *Ultrasonics* **68** 29

[26] Anisimkin V I 2004 *Ultrasonics* **42** 1095
[27] Chambon H, Nicolay P, Bruckner G and Benjeddou A 2017 International Journal of Smart and Nano Materials **8** 95
[28] Caliendo C and Hamidullah M *Journal of Physics D: Applied Physics* **51** 385102
[29] Eguiluz A G and Maradudin A A 1983 Physical Review **28** 728
[30] Pedros, J, Garcia-Gancedo L, Ford C J B, Barnes C H W, Griffiths J P, Jones G A C and Flewitt A J *2011 Journal of Applied Physics* **110** 103501
[31] Hamidullah M, Élie-Caille C and Leblois T 2020 In *2020 IEEE Sensors Proceeding*
[32] Wang T, Mu X, Kropelnicki P, Randles A B and Lee C 2014 **24** 075002
[33] Mu X, Kropelnicki P, Wang Y, Randles A B, Chuan Chai K T, Cai H and Gu Y D 2014 *Applied Physics Letters* **105** 113507
[34] Gerhard Lindner 2008 J. Phys. D: Appl. Phys. 41 123002
[35] Rodríguez-Madrid J G, Iriarte G F, Williams O A and Calle F 2013 *Sensors and Actuators A: Physical* **189** 36